Supporting Information

Low-Temperature Growth of High-Quality Multilayer Graphene Films on Porous CuNi Alloys for Enhanced Corrosion Resistance

Fan Xie, Fan Xia, Zhangyao Xu, Han Han, Ziqi Wang, Qingda Zhu, Haochuan Chen, Fuchao Yan, Yifan Lian, Jingyu Sun, Jincan Zhang*

Supplementary Figures 1-4. Preparation and characterizations of surface-porous CuNi alloy.

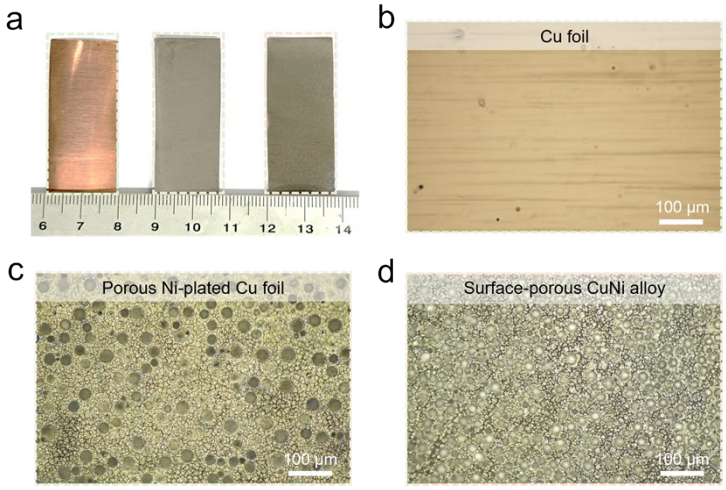

Figure S1. Photographs and optical microscope (OM) characterizations of the three types of samples. (a) Photos of the bare Cu foil (left), the porous Ni-planted Cu foil (middle) and the surface-porous CuNi alloy (right). (b–d) OM images of bare Cu foil (b), the porous Ni-planted Cu foil (c) and the surface-porous CuNi alloy obtained after thermal annealing (d).

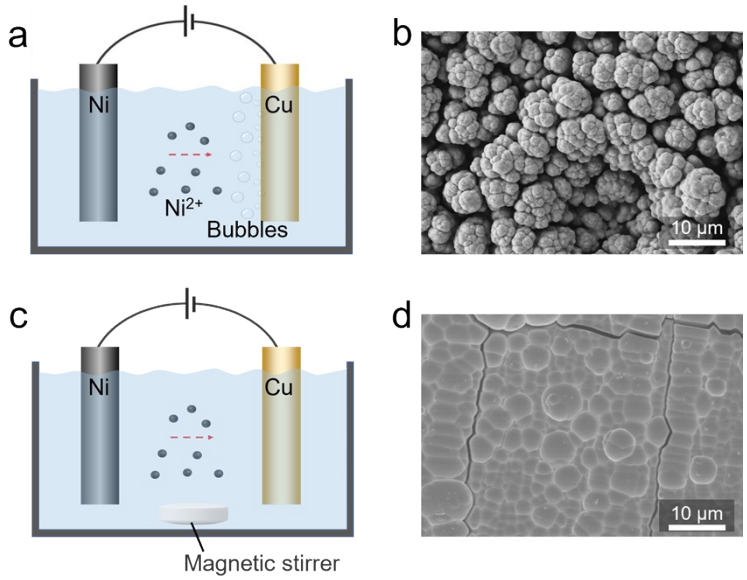

Figure S2. Plating of porous Ni atop Cu substrates. (a) Schematic of the dynamic H_2 bubble template strategy for depositing porous Ni layer on Cu foil. (b) Scanning electron microscope (SEM) image of the porous Ni layer planted on Cu foil. (c) Schematic of the H_2 bubble-free deposition process of Ni on Cu, via magnetic stirring to remove bubbles. (d) SEM images of the Ni layer deposited on Cu foil using the bubble-free strategy.

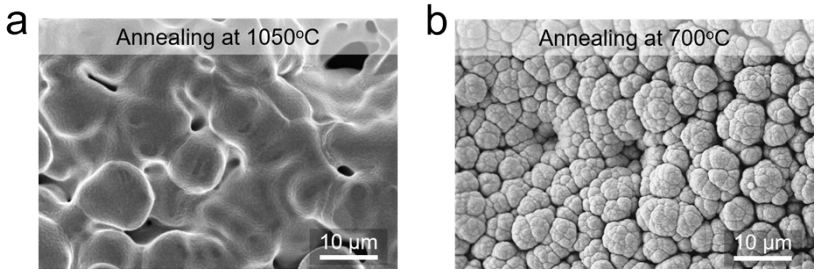

Figure S3. Effect of annealing temperature on surface morphology of the porous CuNi alloy. (a,b) SEM images of the surface after annealing at 1050 °C (a) and at 700 °C (b).

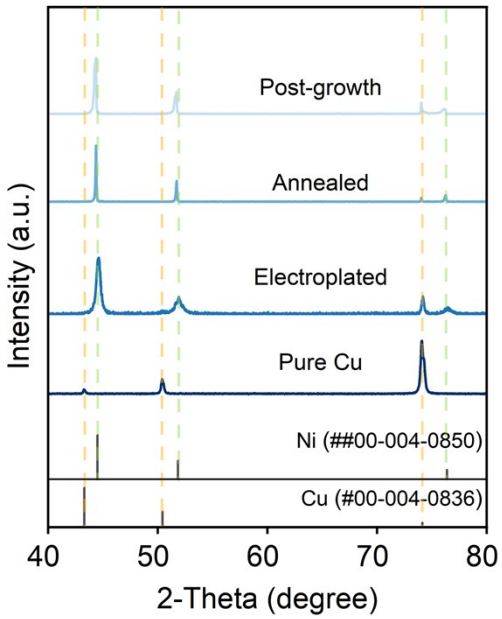

Figure S4. X-ray Diffraction (XRD) patterns of pure Cu foil, the porous Ni planted Cu foil, the surface-porous CuNi alloy, and the graphene-skinned surface-porous CuNi alloy (from bottom to top).

Supplementary Figures 5-8. Low-temperature synthesis of high-quality multilayer graphene (MLG) on surface-porous CuNi alloy.

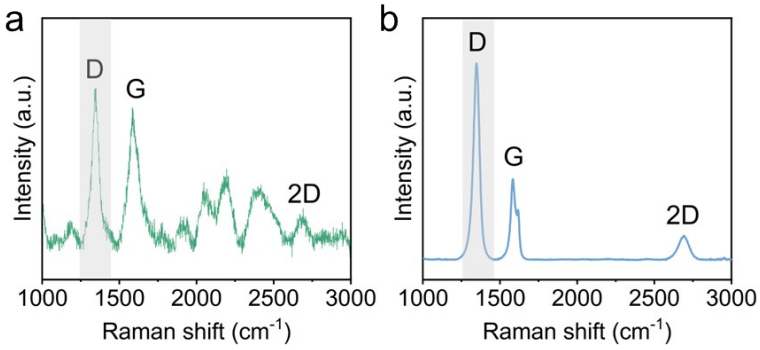

Figure S5. Raman characterization of graphene films synthesized by using methanol as carbon source. (a) Graphene grown on Cu foil at 700°C. (b) Graphene grown on CuNi alloy at 600°C.

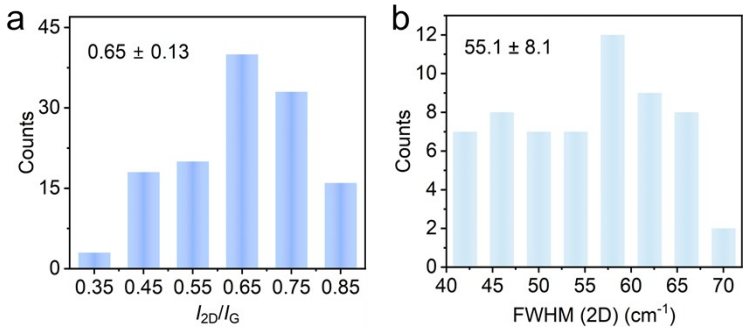

Figure S6. Histogram statistics derived from the Raman line mapping result in Figure 2e. (a) Intensity ratio of 2D to G peaks (I_{2D}/I_G). (b) Full width at half maximum (FWHM) of the 2D peak.

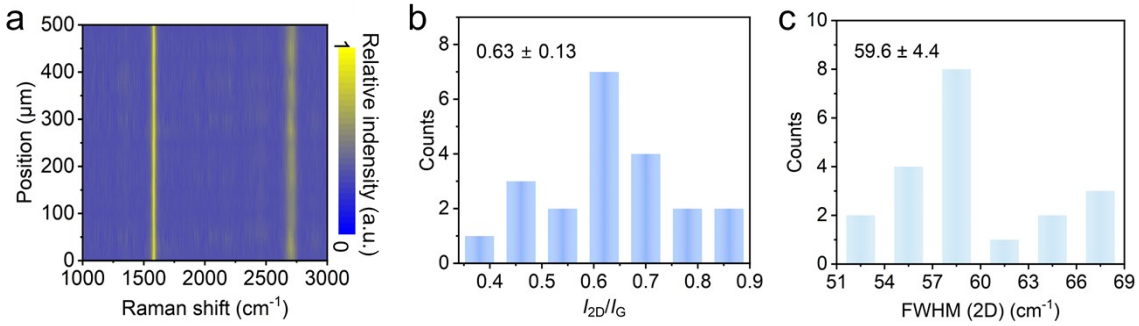

Figure S7. Raman line mapping results of another MLG-skinned surface porous CuNi alloy. (a) Intensity changes of 2D and G peaks within a 500 μm span, with a step size of 25 μm. (b, c) Corresponding histogram statistics of the I_{2D}/I_G (b) and FWHM (2D) (c).

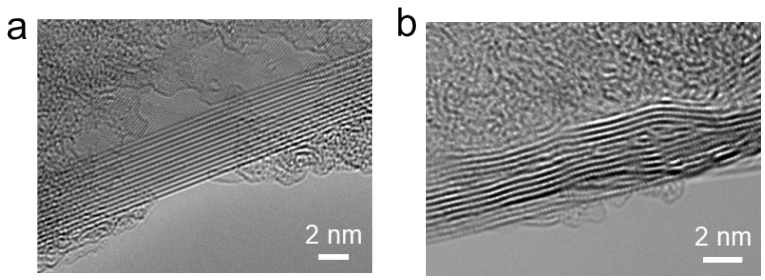

Figure S8. Cross-sectional transmission electron microscopy (TEM) images of the MLG. (a,b) TEM images collected at different positions.

Supplementary Figures 9-13. Electrochemical test of MLG-skinned surface porous CuNi alloy.

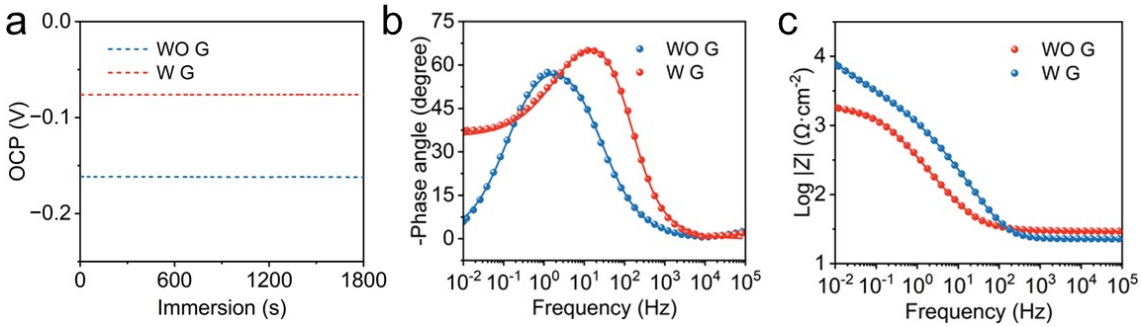

Figure S9. Electrochemical test results of the MLG-skinned and -unskinned surface-porous CuNi alloy. (a) Stabilization of open circuit potential (OCP). (b,c) Electrochemical impedance spectroscopy (EIS) curves showing impact of graphene on the phase angle (b) and lowest frequency impedance modulus ($|Z|_{f=0.01}$) (c).

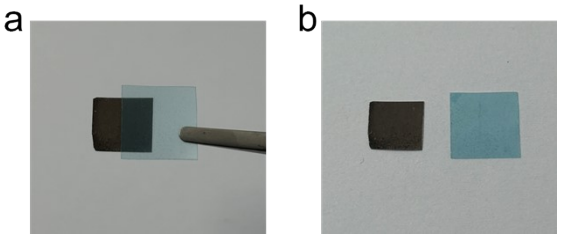

Figure S10. Adhesion stability of graphene. (a) Stick the tape onto the surface of graphene. (b) Peel off the tape.

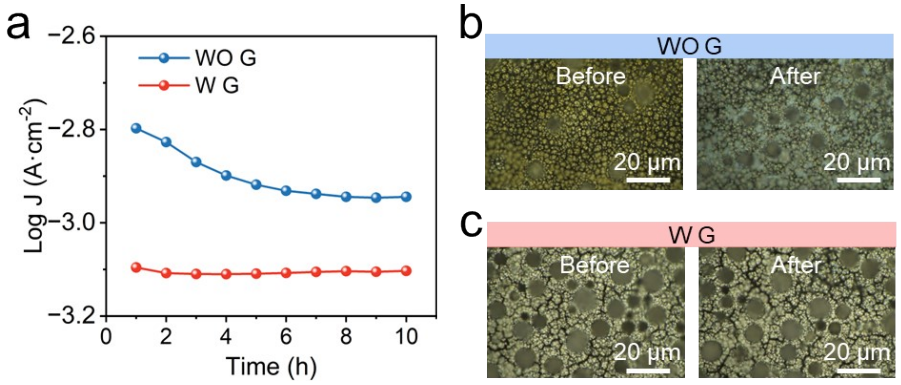

Figure S11. Statistics of corrosion current density during the ten-hour measurement period. (b-c) Optical microscope images of the porous CuNi alloys without (b) and with (c) graphene skins before (left) and after (right) electrochemical tests

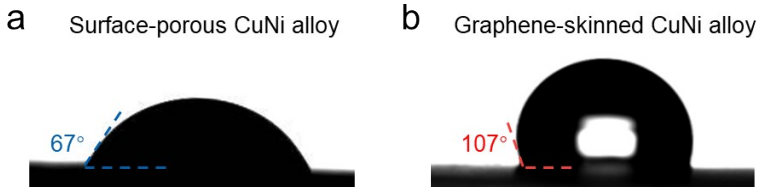

Figure S12. Impact of graphene coverage on the wettability of the porous alloy. (a, b) Water

contact angles of the surface-porous CuNi alloy (a) and the graphene-skinned surface-porous CuNi alloy (b).

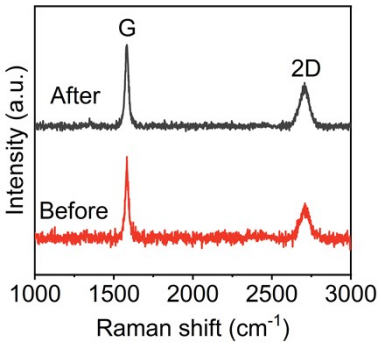

Figure S13. Raman spectra of MLG films on the surface-porous CuNi alloy surfaces before (red) and after (black) electrochemical testing.

Supplementary Figures 14-18. Growth of MLG on bulk-porous CuNi alloy and its corrosion resistance in aqueous environment.

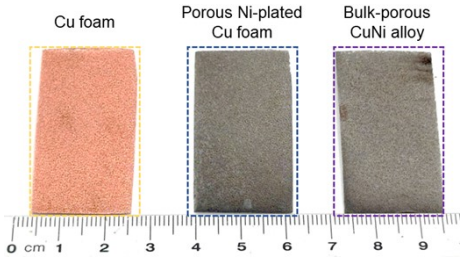

Figure S14. Photographs of the bare Cu foam (left), porous Ni-plated Cu foam (middle), and the bulk-porous CuNi alloy (right).

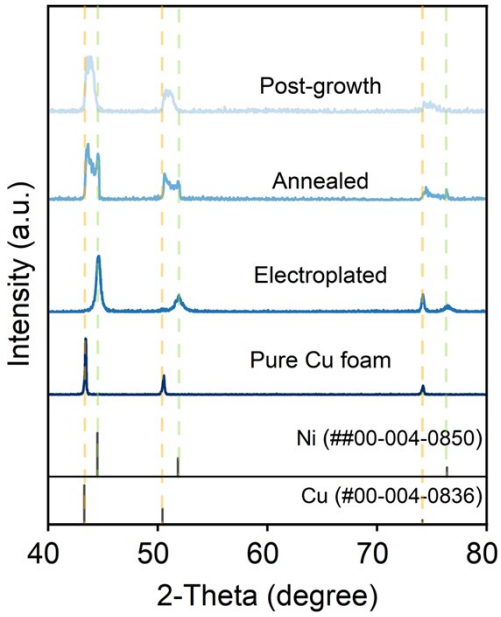

Figure S15. XRD patterns of pure Cu, pure Ni, the bare Cu foam, the porous Ni-planted Cu foam, the bulk-porous CuNi alloy and the MLG-skinned bulk-porous CuNi alloy (from bottom to top).

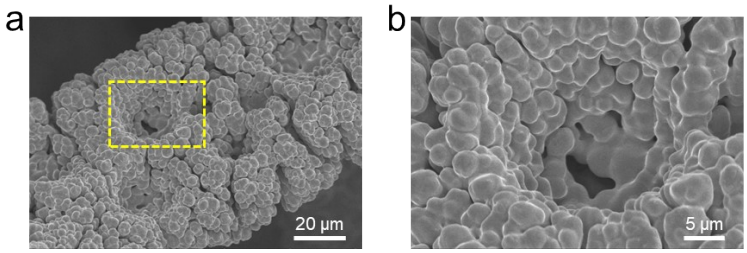

Figure S16. Surface morphology of the MLG-skinned bulk-porous CuNi alloy. (a,b) Typical SEM images, where (b) is the magnified view of the rectangular region marked in (a)

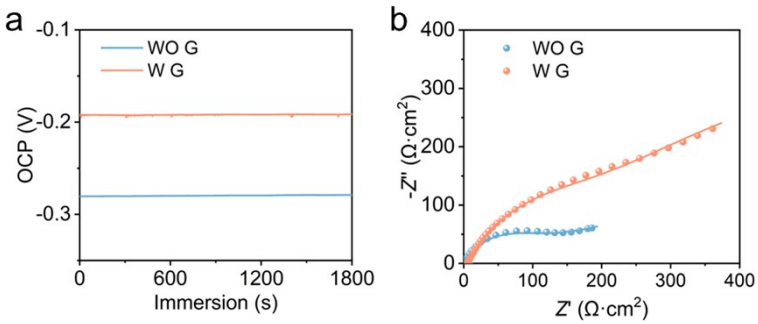

Figure S17. Electrochemical test results of the MLG-skinned and -unskinned bulk-porous CuNi alloys. (a) Stabilization of OCP. (b) EIS curve.

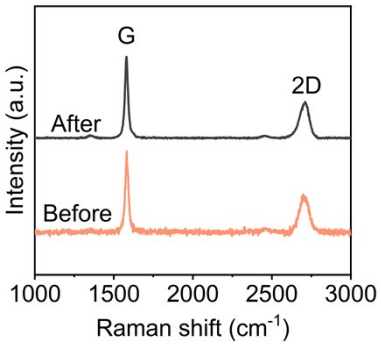

Figure S18. Raman spectra of MLG films on the bulk-porous CuNi alloy surfaces before (orange) and after (black) electrochemical testing.

Table S1. Growth conditions of graphene with CH_3OH or C_2H_5OH as carbon sources.

T_g (°C)	Precursors	Substrates	I_D/I_G	I_{2D}/I_G	Thickness	References
1175	CH_3OH	Carbon fiber	1.01	0.37	/	*Compos. Part B Eng.* **2024**, *273*, 111266
1175	CH_3OH	Carbon fiber	1.03	≤0.10	2L	*Adv. Funct. Mater.* **2024**, *34*, 2409881
1140	CH_3OH	Al_2O_3/SiO_2 skeleton	1.10	0.71	/	*Compos. Part. B-Eng.* **2025**, *289*, 111945
1100	CH_3OH	Si_3N_4 nanowires	0.71	0.72	/	*Chem. Eng. J.* **2024**, *497*, 154307
1100	CH_3OH	Al_2O_3 powder	1.08	0.55	/	*J. Materiomics.* **2025**, *11*, 100999
1060	CH_3OH	Si wafer	0.45	1.22	1L	*Adv. Mater.* **2022**, *34*, 2206389
1050	CH_3OH	SiO_2 fiber	0.64	0.81	11-13L	*Adv. Funct. Mater.* **2024**, *34*, 2411271
1000	C_2H_5OH	Glass	1.14	1.57	1L	*Adv. Mater.* **2017**, *29*, 1603428
1000	CH_3OH	Si_3N_4 nanowire	1.41	0.70	/	*Compos. B Eng.* **2025**, *297*, 112298
1000	CH_3OH	Ni foam	0.59	0.36	2-4L	*Carbon* **2019**, *151*, 109
1000	CH_3OH	h-BN	1.49	0.60	1L	*Appl. Surf. Sci.* **2019**, *475*, 6
800	CH_3OH	$Cu_{81.5}Ni_{18.5}$ foil	0.00	1.22	1L	*Small* **2025**, *21*, 2405854
800	C_2H_5OH	$Cu_{81.5}Ni_{18.5}$ foil	0.6	0.60	/	
700	CH_3OH	$Cu_{80}Ni_{20}$ foil	0.00	0.65	14L	This work

Table S2. Growth conditions of graphene with CuNi alloys as growth substrates.

T_g (°C)	Substrate	Precursors	I_D/I_G	I_{2D}/I_G	Thickness	References
1100	$Cu_{86}Ni_{14}$ foil	CH_4	0.00	0.92	2L	*Nano Res.* **2024**, *17*, 4616
1100	$Cu_{85}Ni_{15}$ foil	CH_4	0.00	1.23	1L	*Nat. Mater.* **2016**, *15,* 43
1075	$Cu_{94.5}Ni_{5.5}$ foil	CH_4	0.00	3.02	1L	*ACS Nano* **2018**, *12,* 6117
1075	$Cu_{81.2}Ni_{18.8}$ foil	CH_4	0.00	1.00	2L	*Nat. Nanotechnol.* **2020,** *15*, 59
1075	$Cu_{81}Ni_{19}$ foil	CH_4	0.00	0.83	1-3L	*Nat. Nanotechnol.* **2020**, *15,* 289
1075	$Cu_{78}Ni_{22}$ foil	CH_4	0.00	1.20	2L	*Chem. Mater.* **2016**, *28, 13,* 4583
1050	$Cu_{88}Ni_{12}$ foil	CH_4	0.00	0.53	2L	*ACS Nano* **2012**, *6,* 7731
1050	$Cu_{85}Ni_{15}$ foil	CH_4	0.00	2.21	1L	*Diam. Relat. Mater.* **2020**, *101*, 107634
1050	CuNi gradient foil	CH_4	0.00	1.27	2L	*ACS Nano* **2018**, *12, 3,* 2275
1000	$Cu_{90}Ni_{10}$ foil	CH_4	0.00	0.67	1L	*Sci. Bull.* **2019**, *64,* 659
1000	$Cu_{90}Ni_{10}$ foil	CH_4	0.00	3.26	1L	*Adv. Funct. Mater.* **2012**, *22,* 1033
1000	$Cu_{80}Ni_{20}$ foil	CH_4	0.00	0.59	2L	*Nano Res*. **2023**, *16*, 10684
1000	$Cu_{75}Ni_{25}$ foil	CH_4	0.00	2.40	1L	*Chem. Mater.* **2014**, *26,* 907
1000	$Cu_{70}Ni_{30}$ foil	CH_4	0.00	0.61	/	*Coatings* **2021**, *11*, 892
1000	$Cu_{68}Ni_{31}$ foil	CH_4	0.00	0.57	/	*Nano Lett.* **2011**, *11*, 3519
1000	$Cu_{20}Ni_{81}$ foil	CH_4	0.00	0.72	/	*CrystEngComm* **2024,** *26,* 2891
800	$Cu_{81.5}Ni_{18.5}$ foil	CH_3OH	0.00	1.14	1L	*Small* **2025**, *21,* 2405854
800	$Cu_{81.5}Ni_{18.5}$ foil	CH_4	0.78	1.01	1L	
757	$Cu_{85}Ni_{15}$ foil	C_2H_4	0.50	1.69	1L	*Nature* **2021**, *596,* 519
750	$Cu_{80}Ni_{20}$ foil	CH_4	0.00	1.68	1L	*Small* **2019**, *15,* 1805395
700	$Cu_{80}Ni_{20}$ foil	CH_3OH	0.00	0.65	14L	This work

Table S3. Corrosion resistance related indicators extracted from electrochemical tests.

Key indicators		**-OCP**	I_{corr}	$-E_{corr}$	R_{ct}	$\|Z\|_{f=0.01\ Hz}$	**η**
Units		**mV**	**μA·cm^{-2}**	**mV**	**Ω·cm^2**	**Ω·cm^2**	**%**
Surface porous	W G	76	0.64	115.9	552	7915.34	93.3
	WO G	162	9.51	190.62	63.6	1735.36	
Bulk porous	W G	191.2	0.93	224.6	158	444	52.3
	WO G	278.9	1.95	377.6	135	184	